Backstepping Supertwisting Control of Four-Phase Interleaved Boost Converter for PEM Fuel Cell

Xinyang Hao, *Graduate Student Member, IEEE*, Issam Salhi, *Member, IEEE*, Salah Laghrouche, Youcef Ait-Amirat, and Abdesslem Djerdir

***Abstract*—This article proposes a novel and robust nonlinear controller for a four-phase interleaved boost converter combined with proton exchange membrane fuel cells. The proposed controller has an inner loop based on a backstepping algorithm, which would transfer the state function of the system to the differential equation of the error variable by using a recursive procedure. The reference current is generated by a supertwisting sliding mode (STSM) algorithm in the outer loop; the sliding surface is defined by the error between the output voltage and reference voltage. The strong robustness and highly dynamic feature of the proposed controller are shown by the performance of the output voltage, source current, and settling time. Besides, the parameters of the proposed controller are tuned and then well optimized using a particle swarm optimization algorithm, and their effectiveness is verified by considering the uncertainty of different operation statuses and the deviations of circuit components. Furthermore, a double-loop STSM controller is chosen for comparison and discussion. The effectiveness of the proposed controller is further evaluated through experimental results obtained with a 500 W fuel cell system based on a real-time hardware-in-the-loop system.**

***Index Terms*—Backstepping controller, fuel cell (FC) applications, interleaved boost converter (IBC), particle swarm optimization (PSO), supertwisting sliding mode (STSM) controller.**

I. Introduction

With the development of the industrial process, fossil fuel still occupies a huge ingredient in energy structure, which would reach approximately 70% in 2050 [1]. However, excessive utilization and burning of fossil fuel for vehicular application have already brought the issues of excessive greenhouse gases emissions, energy shortage, and resource allocation [2]. Over the past two decades, many alternative solutions, such as lithium-ion batteries and hydrogen are gradually applied to hybrid vehicles, which would be a transition to realize 100% defossil fuel [3], [4]. Hydrogen combined with fuel cell (FC) as a chemical energy carrier has become a research hotspot due to its zero emission, high-power energy, and temperature adaptability compared with batteries.

Proton exchange membrane fuel cell (PEMFC) is selected as a prime candidate for vehicle applications because of its excellent performance and stronger environmental adaptability [5]. Since the voltage of a single FC is too low to directly use in practical application, several cells are connected in series to boost voltage. Commonly, the number of cells for an FC stack ranges from hundreds to thousands, which depends on the requirements of voltage and power. However, such an amount of cells would decrease the stability of an FC stack; furthermore, it is hard to maintain the stability of the output voltage for an FC stack, which is caused by the nonlinear characteristics of voltage–current. A dc–dc converter is required to provide a stable voltage and boost FC stack voltage to the desired level.

Among the most sorts of dc–dc converters, two types with voltage boosting functions are the main candidates: isolated and nonisolated converters. The odds of the former are the realization of electrical isolation and theoretically infinite voltage boost ratio. Applications that are not sensitive to the size requirement and need a high-voltage ratio have employed the isolated converter to FC filed [6], [7], such as photovoltaic. Nevertheless, as for vehicle applications, size, cost, and power density are all the consideration factors, which make the isolated converter is not an attractive selection. Theoretically, a standard boost converter as the simplest and cheapest nonisolated converter could be used in FC vehicles, but its simple structure determines that it is not recommended to be employed due to lacking redundancy and no current ripple inhibition ability. An interleaved boost converter (IBC) is constituted by several standard boost converters in parallel; this interleaved topology not only retains the simple structural property of standard boost converter but also solves the issues of redundancy and ripple inhibition, which is recommended as the primary selection for FC vehicles. Therefore, some research articles have been revealed for IBC used in the PEMFC applications [8]–[10].

Nevertheless, it is not an easy task to design a controller for an IBC working for the FC vehicle. On the one hand, many factors need to be considered, such as load disturbance rejection and minimizing the FC current ripple and overshoots. This would bring extra performance requirements for the controller. On the other hand, the nonlinear feature of the FC stack and the ac

Manuscript received October 18, 2021; revised December 26, 2021; accepted January 29, 2022. Date of publication February 9, 2022; date of current version March 24, 2022. This work was supported in part by EIPHI Graduate School under Contract ANR-17- EURE-0002, in part by European Project MobyPost (http://mobypost-project.eu/) funded by the Region Bourgogne Franche-Comté (France) and the FCHJU (European Union), respectively, and in part by Chinese Scholarship Council (CSC - China). Recommended for publication by Associate Editor F. W. Fuchs. *(Corresponding author: Xinyang Hao.)*

The authors are with the Franche-Comté Électronique Mécanique Thermique et Optique-Sciences et Technologies Institute, Université de technologie de Belfort-Montbéliard, Université Bourgogne Franche-Comté, Centre national de la recherche scientifique, École nationale supérieure de mécanique et des microtechniques, F-90000 Belfort, France (e-mail: xinyang.hao@utbm.fr; issam.salhi@utbm.fr; salah.laghrouche@utbm.fr; youcef.ait-amirat@univ-fcomte.fr; abdesslem.djerdir@utbm.fr).

Color versions of one or more figures in this article are available at https://doi.org/10.1109/TPEL.2022.3149099.

Digital Object Identifier 10.1109/TPEL.2022.3149099

component, included in the IBC transfer function from the duty cycle to the output voltage, further increase the difficulty of the controller design. Although a double-loop controller based on proportional–integral (PI) algorithm could satisfy the stability near a certain static operating point [11], it is necessary to design a controller that can meet large wide range stability. Nonlinear controllers have already been reported to solve similar issues for power control in general. Some technologies, such as port-controlled Hamiltonian formulations, Euler–Lagrange, backstepping, and supertwisting sliding mode (STSM), are adopted to regulate the voltage for different converter topologies [12]–[16].

Saadi *et al.* [17] proposed a dual-loop control with H_∞ algorithm for four phases floating IBC (FIBC), which was validated through an FC emulator. Although the effectiveness of the control algorithm has been shown by experiments, it would reduce the persuasions because of a lack of comparison with other control technologies and reliability proof for selected parameters. The different control algorithms with a suitable observer are the research hotspots in recent years, such as flatness control with extended state observer (ESO) in [10] and active disturbance rejection control with ESO in [18], benefiting from the additional observer; extra variable disturbance could be considered, which would further enhance the robustness of the system. Although the above controller is designed for the FC application and shows the expected performance with the experimental results, the shortage is that the FC emulator source is used to replace the FC stack in the experimental validation. A dual-loop PI controller was introduced and verified with IBC for FC in [11]. Hao *et al.* [19] proposed a double-loop supertwisting sliding mode (DL-STSM) control for IBC by considering the performance of FC current, which also shows the good robustness; however, the chattering phenomenon that brings additional ripples to the FC current cannot be eliminated due to the property of sliding mode.

Backstepping control has been developed to stabilize nonlinear dynamical systems [20], [21]. It is a recursive design procedure that links the choice of a control Lyapunov function with the design of a feedback controller and guarantees asymptotic global stability of strict feedback systems [22]. The number of recursive steps depends on the number of state equations of the system designed. In actual application, the state equations of the system would be transferred into the differential equation of inductor current and virtual control law, the corresponding Lyapunov functions are established to complete the stability proof. Some research works have reported that backstepping control is widely used in many fields, especially in photovoltaic systems [23]. The following reasons prompted us to select a backstepping controller in the regulation of the inner loop.

1) Although the recursive technique brings more flexibility for designing [24], complexity is also added if the system has a high order, and it would further lead to a computational burden [25]. Only the current loop is regulated by the backstepping algorithm, which can avoid the calculation for the voltage loop.
2) Even though there is no direct theoretical correlation between employing STSM control and the FC current ripple, Hao *et al.* [19] reveal through the experiments that the STSM control for the inner loop would increase the FC current ripple.
3) Taking into account the demand for rapidity in the inner loop, backstepping control is an effective method to maintain the transient stability of power systems under large disturbances [26], which is very significant for variables that need to change rapidly, such as currents.

Since the STSM algorithm was first proposed, its successive research has covered from the spacecraft to vehicles. Identically, we selected STSM control of the outer loop of the IBC. That is because the following merits are suitable for the output voltage.

1) Considering the robustness requirements of the outer loop, the STSM algorithm as a higher order sliding mode control shows good performance in strong robustness against disturbance and noises [25] compared with other nonlinear controllers.
2) Compared with the traditional ST control, the STSM algorithm can significantly reduce the chattering phenomenon [27].
3) Compared with linear controllers, such as the PI controller, the STSM algorithm is efficient for a large operation range.

In our research, the corresponding sliding surface is set up to the error between the output voltage and the reference voltage, and the control law is the reference current that would be used to constitute the duty cycle in the inner loop. Besides, the stability would be proofed by a candidate Lyapunov function.

In this article, a novel and robust double-loop controller is designed for IBC with FC. The proposed controller structure has two parts: inner loop and outer loop. First, a backstepping control for the inner loop is used to ensure inductor current reference tracking. Then, an STSM control for the outer loop is used to boost FC stack voltage to the desired voltage level. Both controllers' parameters are optimized by using a particle swarm optimization (PSO) algorithm and the robustness of the proposed control system is validated by the uncertainty operation status and changes of circuit parameters.

Although, many controllers based on the different algorithms have been proposed and verified for FC system converter. It is hard to find an equitable method to evaluate each controller, especially for the different nonlinear controllers. Different experimental environments and devices, such as different FC stacks, remaining useful life of the FC stacks, working frequency, converter topologies, and power levels, limit a systematic comparison of different controllers. However, we can still evaluate them from the macroperspective through the number of employed sensors, whether existing stability corroboration, experiments with the use of real FC stack, controller parameters derivation and verification, etc. Table I lists some different controllers that have been proposed in the converters for FC applications. Through the comparison of some macrofactors, the proposed controller not only provides sufficient theoretical support, such as stability certification, parameters derivation, and verification, but also is verified by the FC through setting a fair comparative experiment, which can also be regarded as the advantages. The limitation of the proposed controller is that an additional current sensor for the dc bus is required for the control system. The

TABLE I
DIFFERENT CONTROLLERS USED IN CONVERTERS FOR FC APPLICATIONS

Name	Type	Topology	Sources	Power level	Sensors number	Parameters derivation	Parameters verification	Stability certification	Comparative Experiments
Dual-loop H_∞ algorithm [17]	Nonlinear	FIBC	FC emulator	1.2 kW	Normal	No	No	No	No
Dual-loop PI controller [11]	Linear	IBC	FC	1 kW	Normal	Yes	Yes	Yes	No
Flatness algorithm with ESO [18]	Nonlinear	IBC	FC emulator	240 W	Normal	No	Yes	Yes	Yes
Dual-loop STSM controller [19]	Nonlinear	IBC	FC	500 W	Normal	Yes	No	Yes	Yes
Adaptive backstepping controller [21]	Linear+ Nonlinear	IBC	FC	460 W	Normal	No	No	Yes	Yes
Backstepping Super-twisting sliding mode controller	Nonlinear	IBC	FC	500 W	More	Yes	Yes	Yes	Yes

The bold entities emphasize the controller that is used in this article.

novelty of the proposed controller lies in the adoption of a new structure of inner loop with backstepping and outer loop with STSM, which can further provide strong robustness and a highly dynamic feature. Based on the above analysis, the main contributions of this article can be summarized as follows.

1) A novel robust controller was proposed by combining two different nonlinear control algorithms: backstepping control for the current loop and STSM control for the voltage loop. In addition, theoretical support was provided by the corresponding stability certifications.
2) The PSO algorithm was employed to optimize the best controller parameters by considering errors between the reference value and measurement value of the output voltage and FC current.
3) The effectiveness of the selected controller parameters was verified by taking into account uncertainty operation status and changes of circuit parameters.
4) A 500 W FC system was built for the effectiveness test of the proposed controller. Furthermore, a DL-STSM controller, set with the same parameters optimization method, was used to make a fair comparison.

The rest of this article is organized as follows. The mathematical model of PEMFC, which is predigested by rational assumptions, and the model of four-phase IBC, which is derived from its operation principle, are introduced in Section II. Section III presents the controller design in detail. The specific contents include designing inner- and outer-loop controllers based on the backstepping and STSM algorithms, respectively, the selection and verification of controller parameters, and robustness testing against the different uncertainties. The description of the test bench and experimental results are presented in Section IV. Finally, Section V concludes this article.

II. PEMFC AND FOUR-PHASE IBC MODELING

The FC and its converter are the main components in our research system, and it is necessary to comprehend their working principle and establish their mathematical model. Due to the multiconditional influence and the complexity of modeling for chemical reactions, a common and brief equation FC model is employed based on its working principle. IBC as a sort of kindly energy converter for FC application has been widely used due to its unique characteristics. A nonlinear model for four-phase IBC is built.

A. PEMFC Stack Modeling

Same as other sorts of FC, the reactions that happen in PEMFC are oxidation of H_2 and reduction of O_2, which occur at the PEMFC anode and the PEMFC cathode, respectively [28]

$$\begin{cases} Anode: 2H_2 \rightarrow 4H^+ + 4e^- \\ Cathode: O_2 + 4H^+ + 4e^- \rightarrow 2H_2O + heat. \end{cases} \tag{1}$$

Normally, four layers with different functions are included in PEMFC: flow field plate, gas diffusion electrode, catalyst, and proton exchange membrane. The whole working process of PEMFC needs to consider multidomain knowledge: thermodynamics, electrochemistry, and fluid mechanics, so it is too difficult to establish a precise model for PEMFC when the health condition of PEMFC is further considered. Some research works have been done to find a suitable and precise model for PEMFC [29]; however, building a complex PEMFC model is not the emphasis of this article. A brief model that matches the properties of PEMFC should be employed with the dc–dc converter application.

Essentially, the PEMFC voltage is determined by its current density in a given operating condition [30]. Commonly, three parts are differentiated based on the current density: activation polarization, ohmic polarization, and mass transport loss. Some necessary assumptions would be considered before the PEMFC model is established, which can be referred to the article presented in [31]. A model that considers the computation of the polarization curve and electrochemical impedance around the running point [30] is used in our article. Because the behavior between the two electrodes seems as a supercapacitor, Fig. 1(a) shows the equivalent electrical circuit for PEMFC; where: C is an equivalent capacitor, $r_{\rm act}$, $r_{\rm conc}$, and $r_{\rm ohmic}$ are the equivalent resistances of activation, concentration, and ohmic in PEMFC, respectively, and $E_{\rm Nerst}$ is the reversible potential. Based on the above parameters, the voltage of a PEMFC stack can be expressed as

$$v_{stack} = n\left(E_{Nerst} - \Delta v_{act} - \Delta v_{conc} - \Delta v_{ohmic}\right) \tag{2}$$

where n represents the number of FC monomers.

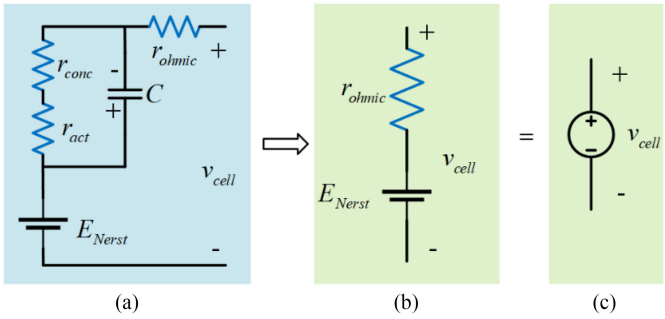

Fig. 1. Equivalent electrical circuit of one single cell. (a) PEMFC equivalent model. (b) Simplified model exceeding 10 kHz. (c) Simplified equivalent model exceeding 10 kHz.

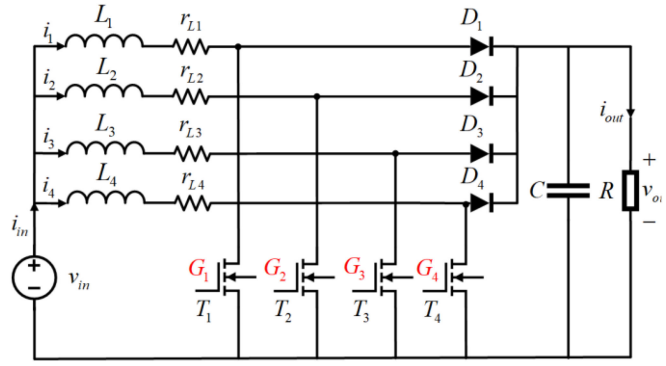

Fig. 2. Topology of four-phase IBC.

The stack ohmic impedance can be considered as a pure and consistent resistance if its working frequency exceeds 10 kHz [32], which would further simplify the proposed model to a dc voltage source and a resistive impedance, which can be shown in Fig. 1(b). For the convenience expression, a voltage source, as shown in Fig. 1(c), can be used to replace the structure in Fig. 1(b).

Two aspects decide the property of PEMFC voltage, which is not primary in the vehicle application. First, the voltage feature of PEMFC is dominated directly by its current; then, the performance of PEMFC current would influence the lifespan of PEMFC. In actual application, a suitable controller would be added to boost the lower PEMFC voltage to a higher constant dc bus voltage within the range of conversion capacity. During this process, the performances of PEMFC current and the dc bus voltage are the main factors to be considered. In total, the model, as shown in Fig. 1(c), can meet the requirements in our research.

B. Four-Phase IBC Modeling

As mentioned in Section I, IBC is selected for FC applications due to the advantages brought by its interleaved structure. As to the specific number of phases, four-phase is a tradeoff selection for the general demand. Two views from the efficiency and inhibition for FC current ripple could account for this issue. The efficiency and inhibition for FC current ripple would be increased when the number of phase increases; however, the corresponding effect would also become unobvious with the increasing phase number. Furthermore, considering the cost brought by more phases, four-phase turns out more suitable for our cases.

Four-phase IBC, as pictured in Fig. 2, has a similar structure and can be considered as four standard boost converter parallel connection. Each boost converter contains an inductor $L_k(k = 1, 2, \ldots, 4)$ with its parasitic resistances $r_{Lk}(k = 1, 2, \ldots, 4)$, a diode $D_k(k = 1, 2, \ldots, 4)$, and a power switch $T_k(k = 1, 2, \ldots, 4)$. C is the common capacitor, f_L is the circuit load, and $v_{\rm in}$ and $i_{\rm in}$ are the PEMFC output voltage and current, $v_{\rm out}$ and $i_{\rm out}$ are the dc bus voltage and current, respectively.

Four-phase IBC works on continuous conduction mode (CCM) based on the interleaved drive signal $G_k(k = 1, 2, \ldots, 4)$ where $T_s/4$ exists between two adjacent phases and the proper inductors sizing. $i_k(k = 1, 2, \ldots, 4)$ are the currents flowing through the inductor L_k and the PEMFC current is the sum of all inductor currents ($i_{\rm in} = i_1 + i_2 + i_3 + i_4$). For the convenience of analysis, the following assumptions are listed as $L_k = L$ and $r_{Lk} = r_k$.

For a standard boost converter, source power would be transferred to the inductor L_k and the capacitor C is discharged through the load if T_k is ON. When T_k is OFF, the source and inductor would charge the capacitor and load simultaneously through the diode D_k. Therefore, the model of four-phase IBC can be obtained based on Kirchhoff's current/voltage law and the above assumptions

$$\begin{cases} \frac{di_k}{dt} = -(1-u_k)\frac{v_{out}}{L} - \frac{r_L}{L}i_k + \frac{r_L}{L}v_{in} \\ \frac{dv_{out}}{dt} = \frac{1}{C}\sum_{k=1}^{4} i_k - \frac{1}{f_L C}v_{out} - \frac{1}{C}\sum_{k=1}^{4} u_k i_k \end{cases} \tag{3}$$

where $u_k(k = 1, 2, \ldots, 4)$ is the duty cycle for switches T_k.

Afterward, the static voltage gain *M(U)* of four-phase IBC in CCM would be obtained by omitting all the losses

$$M(U) = \frac{V_{out}}{V_{in}} = \frac{1}{1-U} \tag{4}$$

where $V_{\rm out}$, $V_{\rm in}$, and U are the average dc values of $v_{\rm out}$, $v_{\rm in}$, and u_k, respectively. Undoubtedly, the features expressed as (3) and (4) can be extended to the application to other phases IBC.

III. Controller Design

In this article, a double-loop control system is designed for four-phase IBC. An outer loop (voltage loop) based on the STSM algorithm is used to ensure the good tracking ability in output voltage and generate the suitable current reference simultaneously. An inner loop (current loop) that uses the backstepping control algorithm is employed to enhance the ability of disturbance rejection and control the FC stack current indirectly. Then, the stability analyses for two loops are proved by using the Lyapunov approach. In addition, the proposed controller parameter selection with their optimization based on the PSO algorithm is presented. Furthermore, their effectiveness is verified by using multiple parameter combinations. Robustness results of the control system against the different uncertainties are shown in Section III-D. In this way, the controller design is divided into four parts, where they are introduced in detail.

A. Backstepping Control for Current Loop

The core scheme of backstepping control is transferring the system state function to the error differential function by establishing the virtual control law. Then, a new error differential function could be certificated by the Lyapunov functions.

Observe that (3) contains four main variables: output voltage $v_{\rm out}$, input voltage $v_{\rm in}$, inductor current i_k, and duty cycle u_k. As mentioned before, due to the property of FC stacks, the input voltage $v_{\rm in}$ depends on the input current. The rest variables should be stabilized asymptotically at $I_{\rm ref}$, $V_{\rm ref}$, and $U_k = 1 - V_{\rm in}/V_{\rm out}$. Equation (5) is established by defining $x_{1k} = i_k$ and $x_2 = v_{\rm out}$ t

$$\begin{cases} \dot{x}_{1k} = -(1-u_k)\frac{x_2}{L} - \frac{r_L}{L}x_{1k} + \frac{r_L}{L}v_{\rm in} \\ \dot{x}_2 = \frac{1}{C}\sum\limits_{k=1}^{4} x_{1k} - \frac{1}{f_L C}x_2 - \frac{1}{C}\sum\limits_{k=1}^{4} u_k x_{1k}. \end{cases} \tag{5}$$

First, the stability of the first state of (5) should be evaluated. Assuming the error z_{1k}, which is the difference between the inductor current and the reference current

$$z_{1k} = x_{1k} - I_{ref} \tag{6}$$

where $I_{\rm ref}$ is produced by the outer loop, and the continuous variable z_{1k} is covered in a range of $[i_{\min} - i_{\max},\ i_{\max} - i_{\min}]$. Combining the derivative equation of inductor current, the dynamics of (6) can be rewritten as

$$\dot{z}_{1k} = -(1-u_k)\frac{x_2}{L} - \frac{r_L}{L}x_{1k} + \frac{r_L}{L}v_{in} - \dot{I}_{_{ref}}. \tag{7}$$

A Lyapunov function is proposed to be

$$V_1(z_{1k}) = \frac{1}{2}\sum_{k=1}^{4} z_{_{1k}}^2 \tag{8}$$

where (8) can satisfy the requirements for a candidate Lyapunov function: $V_1\ (0) = 0$ and $V_1(z_{1k}) > 0$ when $z_{1k} \neq 0$. Afterward, the time derivative of $V_1(z_{1k})$ can be calculated as

$$\dot{V}_1(z_{1k}) = \sum_{k=1}^{4} z_{1k}\dot{z}_{1k}. \tag{9}$$

It is clear to know that $\dot{V}_1(z_{1k}) < 0$ for all $z_{1k} \neq 0$ if a new definition

$$\dot{z}_{1k} = -c_1 z_{1k}, (c_1 > 0) \tag{10}$$

is considered; therefore, the control objective $\lim\limits_{t\to\infty} z_{1k} = 0$ can be fulfilled, which indicates $i_k = I_{ref}$ as well as $t \to \infty$. It is possible to assume that x_2/L is a virtual control law. Its expression can be derived by using $\dot{z}_{1k} = -c_1 z_{1k}$ and further combining (7) as

$$\frac{x_2}{L} := \alpha_k = \left[c_1 z_{1k} - \frac{r_L}{L}x_{1k} + \frac{r_L}{L}v_{in} - \dot{I}_{_{ref}}\right] \Big/ (1-u_i) \tag{11}$$

where the range of α_k is limited between $[X_{2\_\min}/L, X_{2\_\max}/L]$.

As the second step, the objective is to make x_2/L asymptotically approaching α when $t \to \infty$. The error z_2 is defined by using virtual control law as

$$z_{2k} = \frac{x_2}{L} - \alpha_k \tag{12}$$

where the range of z_{2k} resides in $[(v_{out\,\min} - v_{out\,\max})/L, (v_{out\,\max} - v_{out\,\min})/L]$.

Afterward, the time derivative of α_k can be obtained according to (11) as

$$\dot{\alpha}_k = \frac{c_1\dot{z}_{1k} - \ddot{I}_{ref}}{1-u_k} - \frac{r_L\dot{x}_{1k}}{L(1-u_k)} + \frac{\dot{u}_k\alpha_k}{1-u_k}. \tag{13}$$

So, the time derivative of z_2 can be derived by using (5) and (13) as

$$\begin{aligned} \dot{z}_{2k} = {} & \tfrac{1}{LC}\sum_{k=1}^{4}(x_{1k}) - \tfrac{1}{LC}\sum_{k=1}^{4}(u_k x_{1k}) - \tfrac{x_2}{f_L LC} + \tfrac{c_1^2 z_{ak}}{1-u_k} \\ & + \tfrac{\ddot{I}_{ref}}{1-u_k} + \tfrac{r_L\dot{x}_{1k}}{L(1-u_k)} - \tfrac{\dot{u}_k\alpha_k}{1-u_k}. \end{aligned} \tag{14}$$

Up to now, the state space (5) of four-phase IBC has been expressed by the error differential (7) and (14). A candidate Lyapunov function is required to prove the asymptotic stability of z_{2k}, expressively $\lim\limits_{t\to\infty} z_{2k} = 0$. Accordingly, a composite Lyapunov function is proposed as

$$V_2(z_{1k}, z_{2k}) = V_1(z_{1k}) + \frac{1}{2}\sum_{k=1}^{4} z_{2k}^2 \tag{15}$$

where again (15) meets the requirements, i.e., $V_2(0,0) = 0$ and $V_2(z_{1k}, z_{2k}) > 0$ when $z_{1k} \neq 0$, $z_{2k} \neq 0$. Then, the time derivative of $V_2(z_{1k}, z_{2k})$ can be presented by (9) and (10) as

$$\dot{V}_2(z_{1k}, z_{2k}) = \sum_{k=1}^{4}\left\{-c_1 z_{_{1k}}^2 - c_2 z_{2k}^2 + z_{2k}[c_2 z_{2k} + \dot{z}_{2k}]\right\} \tag{16}$$

where $c_2 > 0$ is a parameter that needs to be designed. Note that (16) would be the negative definite if the item between square brackets is equal to zero. In other words

$$c_2 z_{2k} + \dot{z}_{2k} = 0 \tag{17}$$

is the condition that could meet the equilibrium $(z_{1k}, z_{2k}) = (0,0)$ asymptotically. Correspondingly, the control objective of the output voltage v_{out} and the inductor current i_k can be fulfilled at the same time

$$\lim_{t\to\infty} i_k = I_{ref}, \quad \lim_{t\to\infty} v_{out} = V_{ref}. \tag{18}$$

Combining (14) and (17), the duty cycle u_k could be derived as

$$\dot{u}_k = \begin{cases} [c_1^2 - (1-u_k)^2]z_{1k} + [(c_1+c_2)(1-u_k)]\, z_{2k} \\ + \frac{1-u_k}{LC}\sum\limits_{k=1}^{4}[(1-u_k)x_{1k}] - \frac{1-u_k}{f_L LC}x_2 + \ddot{I}_{_{ref}} + \frac{r_L\dot{x}_{1k}}{L} \end{cases} \Big/ \alpha_k. \tag{19}$$

Afterward, the zero dynamics of (19) is necessary to be checked, which could reveal whether or not u_k converges to its equilibrium. In this way, assuming that the four-phase IBC works in a stable state, which would lead to the error variables

z_{1k} and z_{2k} equal to zero. And r_k could be omitted for a better analysis. The following equation can be obtained as:

$$\begin{aligned} x_{1k} &= I_{ref}, \quad x_2 \\ &= V_{ref}, \quad \ddot{I}_{ref} = 0, \quad \alpha_k = V_{in}/[L(1-u_k)]. \end{aligned} \tag{20}$$

Taking (20) into (19), then the controller dynamic can be rewritten as

$$\dot{u}_k = \left[\frac{4(1-u_k)^2}{C} I_{ref} - \frac{1-u_k}{f_L C} V_{ref}\right] \times \frac{1-u_k}{V_{in}}. \tag{21}$$

There are three equilibrium points for u_k by observing (21) if $V_{ref} = V_{out}$ and $I_{ref} = I_{Lk}$ are employed, these are $u_k = 1$ and $u_k = 1 \pm V_{in}/V_{out}$. Only $u_s = 1 - V_{in}/V_{out}$ has actual physical meaning due to $0 < u_k < 1$. Then, (21) could be rewritten at the equilibrium point u_s; the specific operation is that using $(1-u_s)^2 = V_{in}/4 f_L I_{ref}$ replaces the corresponding items. After some derivation, (21) can be represented at u_s

$$\dot{u}_k = \frac{1}{f_L C}\left[\frac{(1-u_k)^3}{(1-u_s)^2} - \frac{(1-u_k)^2}{1-u_s}\right]. \tag{22}$$

Consequently, a linear approximation is adopted around u_s in (22), the last form can be obtained as

$$\dot{u}_k = -\frac{1}{f_L C}\left[u_k - u_s\right]. \tag{23}$$

Note that (23) can easily prove that u_k converges to u_s asymptotically as $t \to \infty$.

B. STSM Control for Voltage Loop

Note that (19) has a parameter I_{ref} that should be provided by the voltage loop. From another side, the control object of the voltage loop is the backstepping controlled IBC as an equivalent plant, and therefore, it is necessary to derive the inner closed-loop transfer function for designing the STSM controller.

Based on (7), by letting $\dot{z}_{1k} = 0$, the equivalent duty cycle u_{eq} can be obtained as follows:

$$u_{eq} = 1 + \frac{\dot{I}_{ref} L - v_{in}}{x_2}. \tag{24}$$

Assuming that the inductors' currents are equal and taking (24) into the last equation of (5), the following relationship can be obtained as:

$$x_2 \frac{dx_2}{dt} = \frac{4x_{1k} v_{in}}{C} - \frac{x_2^2}{f_L C} - \frac{4Lx_1}{C}\frac{dI_{ref}}{dt}. \tag{25}$$

Let the derivative in (25) be zero, and the equilibrium point is obtained as

$$X_{1k} = I_{ref} = \frac{X_2^2}{4 f_L V_{in}}. \tag{26}$$

Using dc component and ac components, such as

$$x_{1k} = X_{1k} + \tilde{x}_{1k}, \quad x_2 = X_2 + \tilde{x}_2, \quad v_{in} = V_{in} + \tilde{v}_{in} \tag{27}$$

to replace the variable in (25) around the equilibrium point, the following equations can be obtained as:

$$X_2 \frac{d\tilde{x}_2}{dt} = \frac{X_2^2 \tilde{v}_{in} + 4\tilde{x}_{1k} V_{in}^2 R}{f_L C V_{in}} - \frac{2X_2 \tilde{x}_2}{f_L C} - \frac{LX_2^2}{f_L C V_{in}}\frac{d\tilde{x}_{1k}}{dt}. \tag{28}$$

Laplace transform is employed to the ac part of (28). The inner closed-loop transfer function can be acquired as

$$G_{ie}|_{v_{in}(s)=0} = \frac{x_2(s)}{x_1(s)} = \frac{a - bs}{s + c} \tag{29}$$

where $a = \frac{4V_{in}}{X_2 C}$, $b = \frac{LX_2}{f_L C V_{in}}$, and $c = \frac{2}{f_L C}$.

As mentioned before, the inner closed loop is considered as an equivalent plant in the progress of designing the voltage loop controller. The input is I_{ref} and output is x_2, then the following equation can be acquired based on (29) as:

$$\dot{x}_2 = -cx_2 + aI_{ref} - b\dot{I}_{ref}. \tag{30}$$

Because (30) is a first-order system, denote $f = -cx_2 - b\dot{I}_{ref}$, the sliding surface $s = x_2 - V_{ref}$ and the control law of STSM

$$I_{ref} = -\beta_1 |s|^{1/2} \mathrm{sgn}(s) - \int \beta_2 \mathrm{sgn}(s) dt \tag{31}$$

the derivative of the sliding surface can be obtained as

$$\dot{s} = \dot{x}_2 = -a\beta_1 |s|^{1/2} \mathrm{sgn}(s) - a\beta_2 \int \mathrm{sgn}(s) dt + f. \tag{32}$$

The necessary proof of outer-loop stability based on the Lyapunov function and Schur theory is presented in the Appendix. The parameters that can satisfy the requirements of asymptotic stability of the outer loop can be limited as

$$\begin{aligned} \beta_1 &> \frac{V_{ref} C}{2V_{in}}, \\ \beta_2 &> \frac{8V_{in}^3 \beta_1^3 + (2V_{in} V_{ref}^2 C^2 \beta_1 - V_{ref}^3 C^3)\delta^2}{8V_{in}^2 \beta_1 (4V_{in}\beta_1 - 2V_{ref} C)} \end{aligned} \tag{33}$$

where δ is defined in the Appendix.

Besides, owing to the parameter I_{ref} needed in the backstepping controller is produced by the outer loop, which would cause a singularity in the final expression of the duty cycle when two loops are combined. Based on (31), the following equations can be obtained:

$$\begin{cases} \dot{I}_{ref} = -\frac{1}{2}\beta_1 |s|^{-1/2} \dot{x}_2 \mathrm{sgn}(s) - \beta_2 \mathrm{sgn}(s) \\ \ddot{I}_{ref} = \left(\frac{1}{4}\beta_1 |s|^{-3/2} \dot{x}_2 - \frac{1}{2}\beta_1 |s|^{-1/2} \ddot{x}_2\right) \mathrm{sgn}(s). \end{cases} \tag{34}$$

From observing (34), $\dot{x}_2$ and $\ddot{x}_2$ are the essential components to constitute $\ddot{I}_{ref}$, $\dot{x}_2$ can be directly obtained by using state-space equation of voltage (5); then, $\ddot{x}_2$ is acquired as

$$\ddot{x}_2 = \frac{1}{C}\left[\sum_{k=1}^{4}\left[(1-u_k)\, x_{1k}\right] - \frac{\dot{x}_2}{R} - \sum_{k=1}^{4}\left(\dot{u}_k x_{1k}\right)\right]. \tag{35}$$

Because of existing $\dot{u}_k$ in the composition of $\ddot{V}_{out}$, which would cause an algebraic loop in (19). In other words, it also influences the selection of outer-loop parameters. Combining

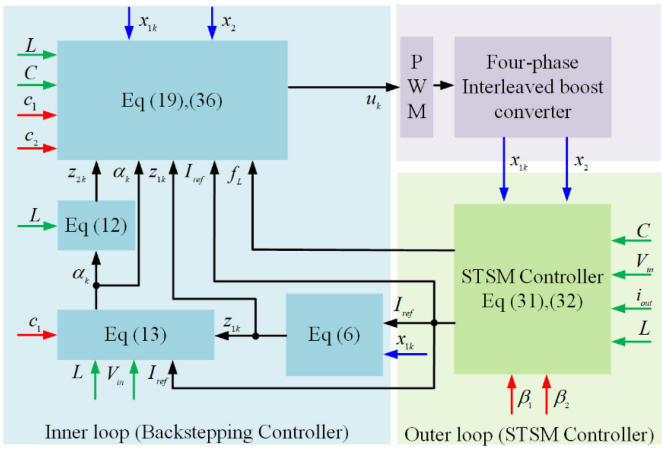

Fig. 3. Control diagram of the proposed closed-loop system for four-phase IBC with FC stack.

(19), (34), and (35), the final expression $\dot{u}_k$ can be obtained by assuming the same operation state in all phases and ignoring r_L

$$\dot{u}_k = \frac{C}{C\alpha_k - 2\beta_1|s|^{-1/2}\mathrm{sgn}(s)x_{1k}} \cdot \Delta \tag{36}$$

where unnumbered equation is shown at the bottom of this page.

It is considered that there is no singularity in (36) if $C\alpha_k \neq 2\beta_1|s|^{-1/2}\mathrm{sgn}(s)x_{1k}$ at all operation times. Therefore, the selection of β_1 is restricted as $\beta_1 \neq C\alpha_k|s|^{1/2}/2\mathrm{sgn}(s)x_{1k}$. α_k has already been defined between $[X_{2\_\min}/L, X_{2\_\max}/L]$, then 10% voltage ripple is considered in the stable condition ($V_{ref} = 48\,V$); thus, β_1 should be selected avoid the range of singularity $[3CX_{2\_\min}/4LI_{\max}, 3X_{2\_\max}/4LI_{\min}]$. In this way, β_1 can be selected to be less than $3CX_{2\_\min}/4LI_{\max}$, finally, the range of β_1 is limited by combining (36) as

$$\frac{V_{ref}C}{2V_{in}} < \beta_1 < \frac{3CV_{out\_\min}}{4LI_{\max}}. \tag{37}$$

Note that (37) depends on the converter parameters and the upper limit of the inductor current, which is related to the employed FC stack.

Fig. 3 shows the diagram of the proposed controller. The relationship between each part and parameters involved in the whole process can be found.

C. Selection and Verification of Controller Parameters

For most nonlinear control algorithms, it is not an easy task to select the corresponding parameters. The methods based on experience are commonly used in solving the parameter issue of nonlinear controllers. However, because of its commonality, it is destined not to be the best solution for parameters and performance of optimization. PSO algorithm as a candidate solution without enough information by simulating the social behavior of birds [33] is employed in this article to deal with this issue. The standard PSO algorithm can be presented as

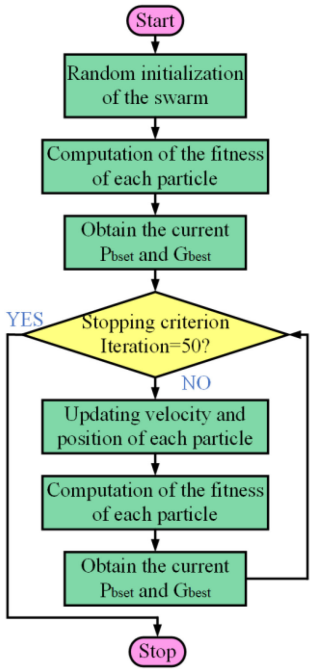

Fig. 4. Flowchart of the proposed PSO algorithm.

$$\begin{cases} v_{k+1} = w \bullet v_k + q_1 \bullet rand() \bullet (P_{best} - p_k) \\ \qquad\quad + q_2 \bullet rand() \bullet (G_{best} - p_k) \\ p_{k+1} = p_k + v_{k+1} \end{cases} \tag{38}$$

where p_k and v_k represent the current position and velocity, and P_{best} and G_{best} are the best position of the current particle and global best position of the whole particles. During the iteration process, the velocity of the particle can adjust itself by the control of the inertia weight w and acceleration constants q_1, q_2. Combining with the control system, four parameters need to be tuned and optimized: c_1, c_2 for the inner loop and β_1, β_2 for the outer loop. Besides, the position is defined as

$$m = \int \left(V_{err}^2 + \sum_{i=1}^{4} I_{i\_err}^2 \right) \bullet t_r dt \tag{39}$$

where V_{err} and I_{err} are the differences between the measured output voltage/inductor current and the reference voltage/inductor current, respectively, and t_r represents the time variable. The flowchart of the proposed PSO algorithm is shown in Fig. 4.

The number of swarms and iteration is set to 50, and m could be obtained by the simulation model. The simulation is established by using MATLAB/Simulink, the sampling frequency of the inductor current is 5 kHz, which is the same as the four-phase

$$\Delta = \left\{ \begin{array}{l} [c_1^2 - (1-u_k)^2]z_{1k} + [(c_1+c_2)(1-u_k)]z_{2k} + \frac{4(1-u_k)^2 x_{1k}}{LC} \\ -\frac{1-u_k}{f_L LC}x_2 + \frac{1}{4}\beta_1|s|^{-3/2}\dot{x}_2^2 - 2\beta_1|s|^{-1/2}(1-u_k)x_{1k}\mathrm{sgn}(s) + \frac{\beta_1\dot{x}_2^2}{2f_L C}|s|^{-1/2} \end{array} \right\}$$

TABLE II
SPECIFICATIONS' PARAMETERS OF THE SYSTEM

Items	Components	Practical Value	Simulation Value
Four-phase IBC	Inductor $L_k(k=1,2,...,4)$	1 mH	
	Parasitic-R $r_{Lk}(k=1,2,...,4)$	3 Ω	
	Capacitor C	6600 μF	
	Frequency f	5 kHz	
	IGBT $T_k(k=1,2,...,4)$	*IXGN120N60A3D1*	Default Model
	Diode $D_k(k=1,2,...,4)$	*BYV541V-200*	Default Model
	Output voltage	40 V~70 V	48 V
Source	Ballard FC Stack	Nominal power 1200W (500 W Real) Nominal voltage: 26 V Operating voltage: 22 V~50 V	DC Power Source 26 V
Load	Electronic load	C100-100-2K	Nominal: 12 Ω
BS+STSM Controller	Outer loop	$\beta_1=0.0027, \beta_2=47.53$	
	Inner loop	$c_1=2970, c_2=6019$	
DL-STSM Controller	Outer loop	$\beta_1=0.0471, \beta_2=95.64$	
	Inner loop	$\beta_3=0.1044, \beta_4=213.2$	

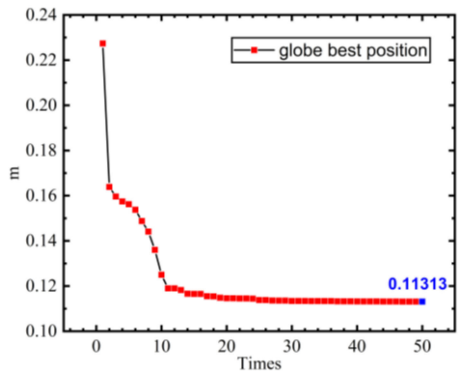

Fig. 5. Trend of the best global position.

IBC operation frequency, and the output voltage sampling frequency is 500 Hz. Additional other circuit parameters used in the simulation are selected based on the actual using components ($V_{\text{in}}=26\,\text{V}$, $L=1000\,\mu H$, $C=6600\,\mu F$, and $V_{\text{out}}=48\,V$); more simulation details can be found in Table II. Besides, the limitation for each parameter should be claimed in the PSO program by considering (33), (38) for the outer loop, and the first step gains c_1 lower than the second step gains c_2 for the inner loop. After 50 times iterations, the trend of the best global position can be obtained, as shown in Fig. 5. The best globe position m declines rapidly at the beginning and then maintains the stability gradually with the number of iterations increasing. Finally, it stops at 0.11313 and the corresponding parameters at

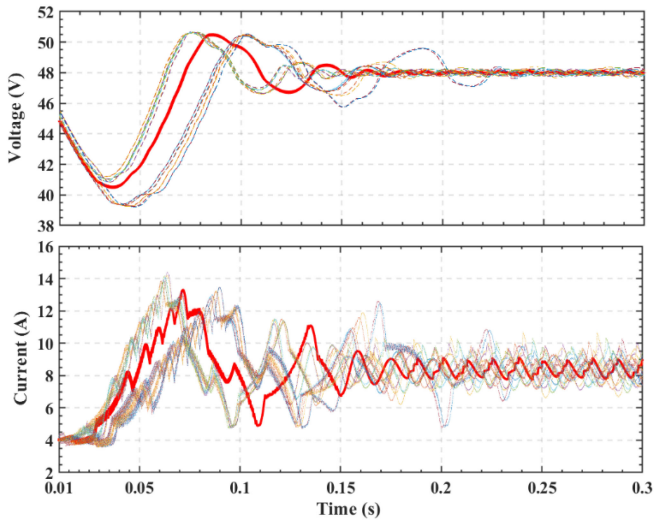

Fig. 6. Simulation results of 16 different parameter combinations.

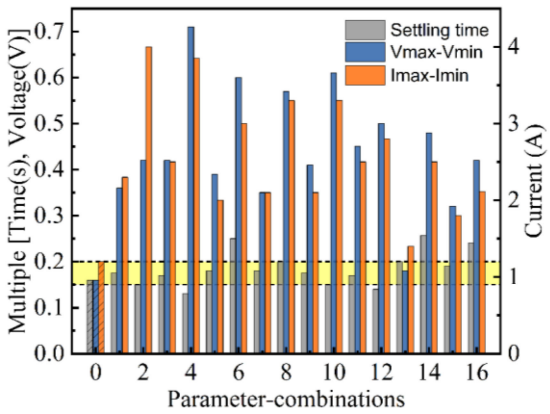

Fig. 7. Simulation results for the important indicators.

this time are: $\beta_1=0.0027$, $\beta_2=47.53$ for the outer loop, and $c_1=2970$ and $c_2=6019$ for the inner loop.

To verify the superiority of the selected controller parameters, different parameter combinations of parameters have been tested and compared with the selected ones. Considering that there are countless parameter combinations within the prescribed range, the fluctuations up and down to 20% at each selected parameter are employed. Therefore, a total of 16 different parameter combinations are used to verify. Fig. 6 shows the performance of the output voltage and input current with the different parameter combinations. The selected parameters demonstrate the good performance that makes a tradeoff between rapidity and stability, which is represented in the red line, as shown in Fig. 6.

In order to clearly show the performance brought by the different parameter combinations, Fig. 7 are sorted from the settling time, the error of the output voltage $\Delta v_{\text{out}}(v_{\text{out max}}-v_{\text{out min}})$, and the error of the input current $\Delta i_{\text{in}}(i_{\text{in max}}-i_{\text{in min}})$. The left *Y*-axis contains the output voltage and settling time; the right *Y*-axis is the input current. The abscissa "0" represents the selected parameters and "1"–"16" are 16 different parameter combinations. It can be concluded that parameter combinations "10" and "12" have the faster settling time but fail in the ripple

control of the voltage and current; parameter combination "13" shows a relatively balanced performance. The selected parameters reduce the ripple of the voltage and current greatly with a fast and acceptable stabilization time compared with other parameter combinations.

D. Robustness Testing of Control System Against the Uncertainty

To verify the effectiveness and robustness of the proposed controller, two types of uncertainty conditions should be considered. One of the uncertainties is brought by the change of converter operating status, such as the different input voltages and levels of load power. Second, the deviations of circuit components can lead to uncertainty, which is caused by the manufacture and aging of inductors or capacitors.

For comparison purposes, a double-loop super-twisting sliding mode (DL-STSM controller is chosen by replacing the backstepping controller in the current loop with another STSM controller. Two reasons illustrate why the DL-STSM is selected. First, the DL-STSM controller could provide good robustness with a reasonable ripple limitation of input current for the FC application; second, it shows the inhibition ability for overshoot of the FC current [20]. For a fair comparison, the parameters selection of the DL-STSM controller still utilizes the PSO algorithm for better optimization. It is worth noting that the parameters of the outer loop cannot be the same as the proposed controller, although the same control algorithm is employed to the outer loop, that is because the singularity does not need to be considered in this situation. The solution is $\beta_1 = 0.0471$, $\beta_2 = 95.64$ for the voltage loop and $\beta_3 = 0.1044$, $\beta_4 = 213.2$ for the current loop. The same sampling time and nominal components value are kept with Section III-C. The parameters calculated by PSO algorithm are employed in two different controllers to verify their respective robustness against the uncertainty.

To verify the controller robustness to handle the uncertainty with a variable converter operating point, five different representative operations are selected, which are shown in Fig. 8. The performances of the output voltage with the proposed controller and DL-STSM controller are presented in Fig. 8(a) and (b), respectively. It can be clearly observed that the proposed controller almost shows the same output performance under the smaller overshoot and the faster settling time compared with the DL-STSM controller. The maximum overshoot is 3.32 V and the settling time is 0.15 s for the DL-STSM controller; in comparison, a 60% reduction in output voltage overshoot (1.31 V) and 33% reduction in settling time (0.1 s) are achieved by the proposed controller.

To verify the controller robustness to deal with the uncertainty related to the changed circuit parameter, circuit parameters change with a 20% fluctuation from the nominal value, as shown in Fig. 9. The performances of the output voltage with the proposed controller and DL-STSM controller are presented in Fig. 9(a) and (b), respectively. Two conclusions can be obtained: first, both controllers show almost the same performance in terms of settling time; second, the proposed controller has better inhibition capability in output voltage compared with DL-STSM controller (0.88 V versus 1.88 V).

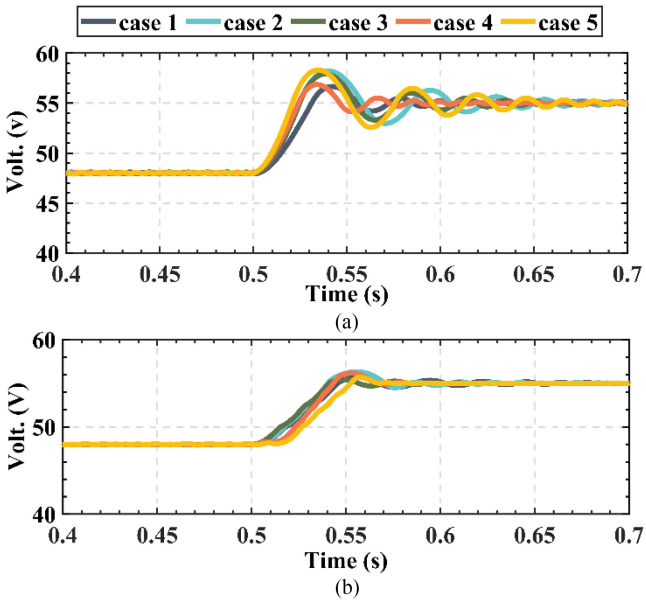

Fig. 8. Simulation results of the output voltage with the different operation points. Case 1: $V_{\text{in}} = 22$ V, load $= 6\ \Omega$; case 2: $V_{\text{in}} = 22$ V, load $= 15\ \Omega$; case 3: $V_{\text{in}} = 26$ V, load $= 12\ \Omega$; case 4: $V_{\text{in}} = 30$ V, load $= 6\ \Omega$; case 5: $V_{\text{in}} = 30$ V, load $= 15\ \Omega$. (a) DL-STSM controller. (b) Proposed controller.

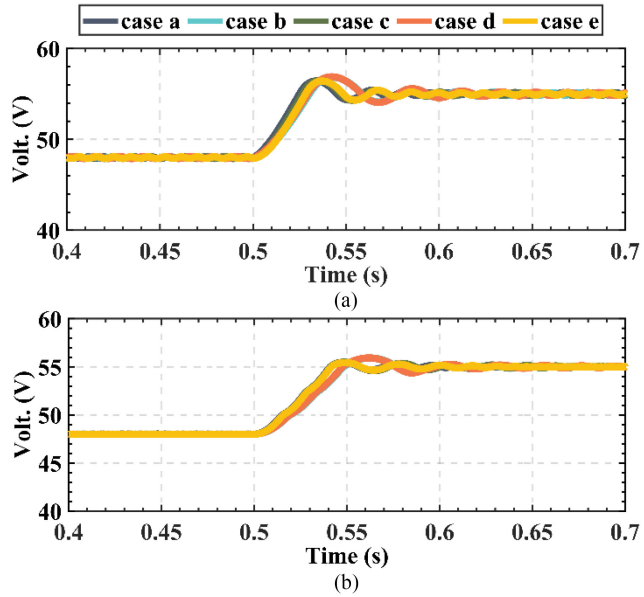

Fig. 9. Simulation results of the output voltage with the changed circuit parameters. Case a: $L = 800\ \mu$H, $C = 5200\ \mu$F; case b: $L = 800\ \mu$H, $C = 5200\ \mu$F; case c: $L = 800\ \mu$H, $C = 5200\ \mu$F; case d: $L = 800\ \mu$H, $C = 5200\ \mu$F; case e: $L = 800\ \mu$H, $C = 5200\ \mu$F. (a) DL-STSM controller. (b) Proposed controller.

IV. Experimental Results and Discussion

To validate the correctness of the proposed four-phase IBC and the effectiveness of the controller concerning load disturbance and the variable reference voltage, an experimental platform was built based on the structure of Fig. 10.

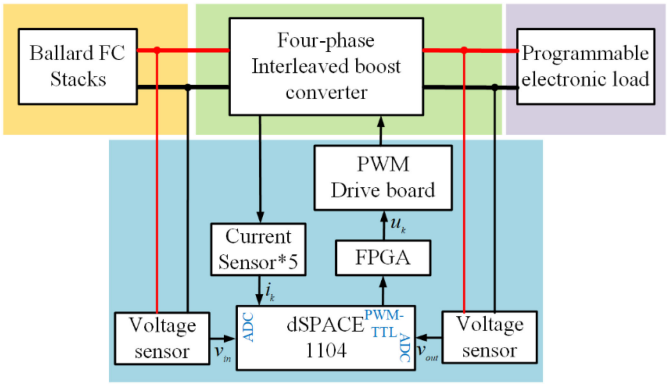

Fig. 10. Experimental setup structure.

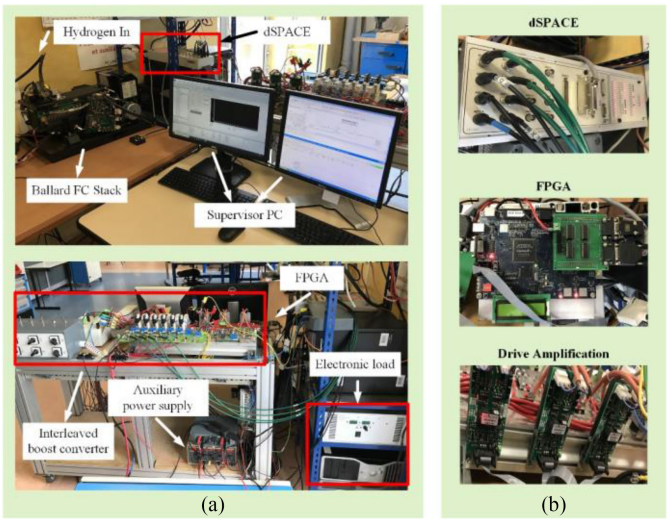

Fig. 11. Experimental test bench. (a) Overall picture of the experimental test bench. (b) Interface circuit for drive signal generating and amplification.

A. Experimental System Description

The experimental system consists of four parts: Ballard FC, four-phase IBC, pulsewidth modulation (PWM) generation, and the load part, which are shown in Fig. 11. The FC stack is Ballard *310-0027-02*, and its nominal voltage and current are 26 V and 46 A, respectively.

However, the maximum power of the FC stack is limited to 500 W by considering the performance degradation due to long-term operation. As for four-phase IBC, the IGBT *IXGN120N60A3D1* with up to 5 kHz switching frequency capability is used, which further determines converter working frequency to 5 kHz. Besides, the inductor value $L = 1000\,\mu H$ was used to ensure CCM and reduce the inductor current ripple. The rest components are listed in Table II.

PWM generation part contains *dSPACE1104*, *FPGA EPC12Q240C8*, and the drive board. The controller could be performed in dSPACE1104 and produce four PWM signals with the same phase. FPGA is used to phase shift by $T_k/4$ two adjacent PWM signals. Finally, the drive board (*ARCAL2108* and *2SC0108T2G0-17*) amplifies the shifted PWMs to signals G_k that meet the IGBTs drive requirements. As for the load part, there is a programmable electronic load (model is *C100-100-2K*), which can be utilized by setting the value of absorbed current.

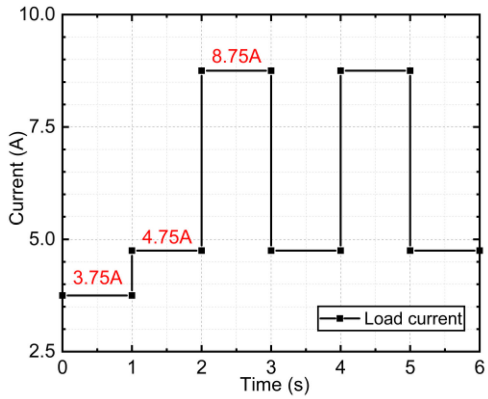

Fig. 12. Variation waveform of the load current.

Four inductor currents and output current are measured by hall current sensor *LA55-P*; the input and output voltage are obtained by two-channel differential probe *MTX 1032-B*. Afterward, the controller would implement its function based on the above-collected values. The oscilloscope model is Tektronix *TBS 2000B*, and the current probe is *Fluke 801-110S*. It is worth noting that the sampling frequency is set to 5 kHz for the current and 500 Hz for the voltage.

B. Step Load Disturbance

The load is not always constant in the vehicle application, which needs to start and stop frequently. Therefore, studied controllers were tested experimentally to evaluate their ability to keep the output voltage constant despite consumed power variations. Therefore, the reference voltage is fixed at 48 V during the test of step load disturbance; then, the programmable electronic load is employed to change the load every 1 s, which is set in Fig. 12 beforehand. Fig. 13 shows the experimental results when the output voltage is set to $V_{ref} = 48\,V$ under step load disturbance.

The evolution of the voltages (currents) at the input and output of the IBC is revealed, as shown in Fig. 13. During the experiment, five load disturbances are carried out via the electronic load: once load increases of 1 A (48 W), twice load increases of 4 A (192 W), and twice load decreases of 4 A (192 W). The controller could maintain stable output voltage and inhibit input current overshoot within a short time when suffering steps load disturbance. From the results, both controllers reveal good inhibition ability for the FC current overshoot, which would help to protect FC stacks and extend their lifespan. It can be observed that at the transient performance, with DL-STSM controller, the output voltage varieties are 8.2 and 16 V for 192 W step load disturbance; besides, their corresponding settling times are 350 and 440 ms. In contrast, with the proposed controller, the output voltage varieties are 1.3 and 2.2 V, with the corresponding settling time of 95 and 110 ms. It can also be shown that the

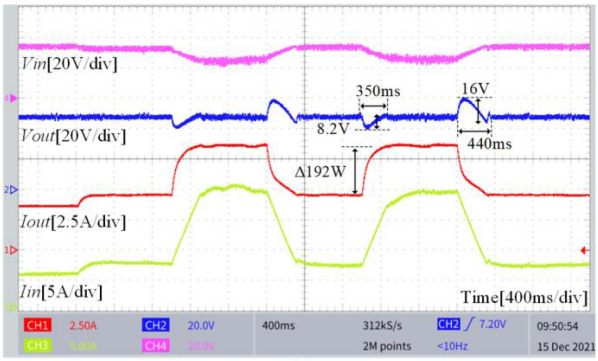

(a)

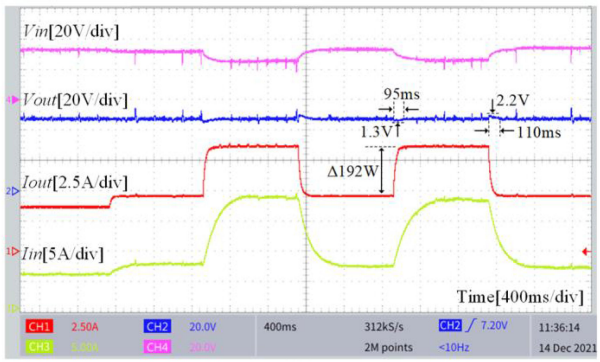

(b)

Fig. 13. Experimental results of four-phase IBC under step load disturbance $V_{ref} = 48\,V$. (a) DL-STSM controller. (b) Proposed controller.

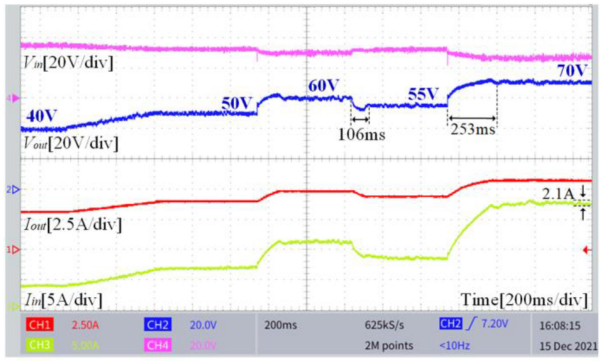

(a)

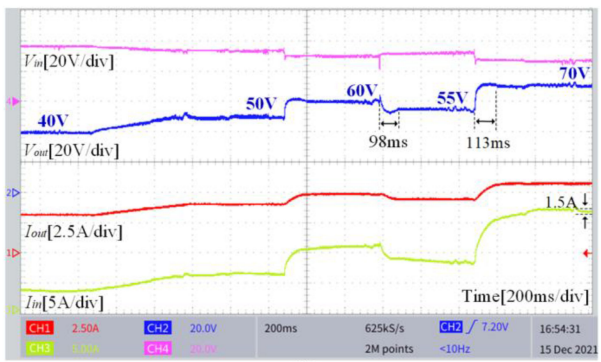

(b)

Fig. 15. Experimental results with a variable reference voltage. (a) DL-STSM controller. (b) Proposed controller.

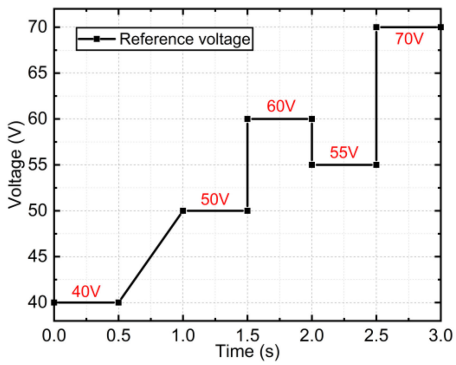

Fig. 14. Variation waveform of the reference voltage.

proposed controller has a better ripple inhibition ability for the output voltage versus the DL-STSM controller.

C. Variable Reference Voltage

Even though the power converter designed for vehicle applications has a fixed dc bus voltage to a given level; nevertheless, the proposed controller is designed to ensure that output voltage could converge to reference voltage with the different voltage levels. In this way, a variable reference voltage is set from 40 to 70 V with a specific profile with a fixed load, which is shown in Fig. 14.

Fig. 15 shows experimental results with a variable reference voltage. As it can be seen from those figures, the effect of the DL-STSM controller and the settling time of 106 and 253 ms are insured when the reference changes as a step from 60 to 55 V and from 55 to 70 V, respectively. In contrast, the proposed controller provides a faster settling time with 98 and 113 ms for the same step. Besides, the proposed controller shows a better performance in terms of both FC current ripple and output voltage ripple.

From the above experiments, the proposed controller has a better transient performance in load disturbance where the output voltage has a smaller overshoot and undershoot. Besides, the smaller ripple also appears in the FC stack current. The experimental results of variable reference voltage are involved in leading to the same conclusion.

V. Conclusion

Taking into account the robustness of the output voltage and the performance of the PEMFC current, which contains ripple and overshoot, a novel and robust nonlinear controller is designed for a four-phase IBC working with PEMFC. The proposed controller contains backstepping control for the inner loop and STSM control for the outer loop. The following control objectives are achieved: stable output voltage with different levels, strong load disturbance rejection ability, and inhibition ability of PEMFC current ripple. First of all, the mathematical model of PEMFC based on the assumptions of the ideal operating conditions and the state function of four-phase IBC based on Kirchhoff's law are introduced. Afterward, the design of the proposed controller was presented in detail from the following four aspects: inner-loop controller design, outer-loop controller

design, parameter selection based on PSO algorithm, and robustness validation for the control system against the uncertainty by considering different operation statuses and changed circuit parameters. Finally, an experimental test bench based on a PEMFC system with four-phase IBC was built to verify the effectiveness of the controllers by using dSPACE and FPGA boards.

All in all, the proposed controller has better performance in terms of robustness of the output voltage, settling time, and ripple inhibition of the PEMFC current compared with the DL-STSM controller, which would not only improve the quality of dc bus voltage but also extend the lifespan of PEMFC.

APPENDIX

Some substitutions, $w = -a\beta_2 \int \mathrm{sgn}(s)dt + f$, $k_1 = a\beta_1$, and $k_2 = a\beta_2$, are used in (32); therefore, (32) can be rewritten as

$$\begin{cases} \dot{s} = -k_1|s|^{1/2}\mathrm{sgn}(s) + w \\ \dot{w} = -k_2\mathrm{sgn}(s) + \dot{f} \end{cases} \tag{a1}$$

A candidate Lyapunov function $V_3(\xi_1, \xi_2)$ is established to prove s could converge to zero as $t \to \infty$, which, therefore, illustrate the output voltage $x_2(v_{out})$ approaches V_{ref}

$$V_3(\xi_1, \xi_2) = \xi^T P \xi \tag{a2}$$

where $\xi^T = [\,\xi_1\ \xi_2\,] = [\,|s|^{1/2}\mathrm{sgn}(s)\ w\,]$ and $P = \frac{1}{2}\begin{bmatrix} k_1^2+4k_2 & -k_1 \\ -k_1 & 2 \end{bmatrix}$.

$V_3(\xi_1, \xi_2)$ can be expanded to $\frac{1}{2}[4k_2\xi_1^2 + (k_1\xi_1 - \xi_2)^2 + \xi_2^2]$; the latter is positive if $k_2 > 0$ when $\xi_1 \neq 0$ and $\xi_2 \neq 0$. In addition, $V_3(0, 0) = 0$. The derivative of ξ can be acquired by calculation

$$\dot{\xi} = (1/|\xi_1|)\,(A \cdot \xi + B \cdot \psi) \tag{a3}$$

where $A = \begin{bmatrix} -\frac{k_1}{2} & \frac{1}{2} \\ -k_2 & 0 \end{bmatrix}$, $B = \begin{bmatrix} 0 \\ 1 \end{bmatrix}$, and $\psi = |s|^{1/2}\dot{f}$.

Therefore, the derivative of $V_3(\xi_1, \xi_2)$ can be expanded as

$$\begin{aligned} \dot{V}_3(\xi_1, \xi_2) &= \dot{\xi}^T P \xi + \xi^T P \dot{\xi} \\ &= \frac{1}{|\xi_1|}[\xi^T A^T P \xi + \psi^T B^T P \xi + \xi^T P A \xi + \xi^T P B \psi] \\ &= \frac{1}{|\xi_1|}\begin{bmatrix} \xi \\ \psi \end{bmatrix}^T \begin{bmatrix} A^T P + PA & PB \\ B^T P & 0 \end{bmatrix} \begin{bmatrix} \xi \\ \psi \end{bmatrix} \\ &\le \frac{1}{|\xi_1|}\left\{ \begin{bmatrix} \xi \\ \psi \end{bmatrix}^T \begin{bmatrix} A^T P + PA & PB \\ B^T P & 0 \end{bmatrix} \begin{bmatrix} \xi \\ \psi \end{bmatrix} + {\xi_1}^2\delta^2 - \psi^2 \right\} \\ &= \frac{1}{|\xi_1|}\begin{bmatrix} \xi \\ \psi \end{bmatrix}^T \begin{bmatrix} A^T P + PA + \delta^2 C^T C & PB \\ B^T P & -1 \end{bmatrix} \begin{bmatrix} \xi \\ \psi \end{bmatrix} \\ &\le -(1/|\xi_1|)\,\xi^T Q \xi \end{aligned} \tag{a4}$$

where $Q = -(A^T P + PA + \delta^2 C^T C + PBB^T P)$, $C = [\,1\ 0\,]$, and δ is an auxiliary variable, its value should satisfy $\delta \ge |\dot{f}|$.

Note (a4) that $V_3(\xi_1, \xi_2)$ would be negative definite if Q is a positive definite matrix. Based on Schur theory, the conditions that satisfy a positive definite matrix Q can be obtained as

$$k_1 > 2, k_2 > \frac{k_1^3 + 4(k_1 - 2)\delta^2}{4k_1(k_1 - 2)}. \tag{a5}$$

Combining the relationship between k_i and β_i, (33) can be obtained.

REFERENCES

[1] E. L. V. Eriksson and E. M. A. Gray, "Optimization and integration of hybrid renewable energy hydrogen fuel cell energy systems—A critical review," *Appl. Energy*, vol. 202, pp. 348–364, 2017.

[2] M. S. Bhaskar, V. K. Ramachandaramurthy, S. Padmanaban, F. Blaabjerg, and M. Mitolo, "Survey of dc–dc non-isolated topologies for unidirectional power flow in fuel cell vehicles," *IEEE Access*, vol. 8, pp. 178130–178166, 2020.

[3] Q. Wang, M. Xue, B.-L. Lin, Z. Lei, and Z. Zhang, "Well-to-wheel analysis of energy consumption, greenhouse gas and air pollutants emissions of hydrogen fuel cell vehicle in China," *J. Cleaner Prod.*, vol. 275, 2020, Art. no. 123061.

[4] M. Carignano, V. Roda, R. Costa-Castelló, L. Valiño, A. Lozano, and F. Barreras, "Assessment of energy management in a fuel cell/battery hybrid vehicle," *IEEE Access*, vol. 7, pp. 16110–16122, 2019.

[5] A. Alyakhni, L. Boulon, J.-M. Vinassa, and O. Briat, "A comprehensive review on energy management strategies for electric vehicles considering degradation using aging models," *IEEE Access*, vol. 9, pp. 143922–143940, 2021.

[6] T. Hong, Z. Geng, K. Qi, X. Zhao, J. Ambrosio, and D. Gu, "A wide range unidirectional isolated dc–dc converter for fuel cell electric vehicles," *IEEE Trans. Ind. Electron.*, vol. 68, no. 7, pp. 5932–5943, Jul. 2021.

[7] X. Pan, H. Li, Y. Liu, T. Zhao, C. Ju, and A. Kumar Rathore, "An overview and comprehensive comparative evaluation of current-fed-isolated-bidirectional dc/dc converter," *IEEE Trans. Power Electron.*, vol. 35, no. 3, pp. 2737–2763, Mar. 2020.

[8] K. J. Reddy and N. Sudhakar, "High voltage gain interleaved boost converter with neural network based MPPT controller for fuel cell based electric vehicle applications," *IEEE Access*, vol. 6, pp. 3899–3908, 2018.

[9] B. Mallikarjuna Reddy and P. Samuel, "Analysis, modelling and implementation of multi-phase single-leg dc/dc converter for fuel cell hybrid electric vehicles," *Int. J. Model. Simul.*, vol. 40, no. 4, pp. 279–290, 2020.

[10] Y. Huangfu, Q. Li, L. Xu, R. Ma, and F. Gao, "Extended state observer based flatness control for fuel cell output series interleaved boost converter," *IEEE Trans. Ind. Appl.*, vol. 55, no. 6, pp. 6427–6437, Nov./Dec. 2019.

[11] S. Somkun, C. Sirisamphanwong, and S. Sukchai, "A DSP-based interleaved boost dc–dc converter for fuel cell applications," *Int. J. Hydrogen Energy*, vol. 40, no. 19, pp. 6391–6404, 2015.

[12] P. Mungporn *et al.*, "Modeling and control of multiphase interleaved fuel-cell boost converter based on Hamiltonian control theory for transportation applications," *IEEE Trans. Transport Electrific.*, vol. 6, no. 2, pp. 519–529, Jun. 2020.

[13] K. Shipra, R. Maurya, and S. N. Sharma, "Port-controlled Hamiltonian-based controller for an interleaved boost PFC converter," *IET Power Electron.*, vol. 13, no. 16, pp. 3627–3636, 2020.

[14] N. Agrawal, S. Samanta, and S. Ghosh, "Modified LQR technique for fuel-cell-integrated boost converter," *IEEE Trans. Ind. Electron.*, vol. 68, no. 7, pp. 5887–5896, Jul. 2021.

[15] K. Behih and H. Attoui, "Backstepping terminal sliding mode MPPT controller for photovoltaic systems," *Eng., Technol. Appl. Sci. Res.*, vol. 11, no. 2, pp. 7060–7067, 2021.

[16] S. M. Rakhtala and A. Casavola, "Real-time voltage control based on a cascaded super twisting algorithm structure for dc–dc converters," *IEEE Trans. Ind. Electron.*, vol. 69, no. 1, pp. 633–641, Jan. 2022.

[17] R. Saadi, M. Y. Hammoudi, O. Kraa, M. Y. Ayad, and M. Bahri, "A robust control of a 4-leg floating interleaved boost converter for fuel cell electric vehicle application," *Math. Comput. Simul.*, vol. 167, pp. 32–47, 2020.

[18] S. Zhuo, L. Xu, Y. Huangfu, A. Gaillard, D. Paire, and F. Gao, "Robust adaptive control of interleaved boost converter for fuel cell application," *IEEE Trans. Ind. Appl.*, vol. 57, no. 6, pp. 6603–6610, Nov./Dec. 2021.

[19] X. Hao, I. Salhi, S. Laghrouche, Y. Ait-Amirat, and A. Djerdir, "Robust control of four-phase interleaved boost converter by considering the performance of PEM fuel cell current," *Int. J. Hydrogen Energy*, vol. 46, no. 78, pp. 38827–38840, 2021.
[20] Y. Jin *et al.*, "A dual-layer back-stepping control method for Lyapunov stability in modular multilevel converter based STATCOM," *IEEE Trans. Ind. Electron.*, vol. 69, no. 3, pp. 2166–2179, Mar. 2022.
[21] Y. A. Zúñiga-Ventura, D. Langarica-Cordoba, J. Leyva-Ramos, L. H. Díaz-Saldierna, and V. M. Ramírez-Rivera, "Adaptive backstepping control for a fuel cell/boost converter system," *IEEE J. Emerg. Sel. Topics Power Electron.*, vol. 6, no. 2, pp. 686–695, Jun. 2018.
[22] S. Vaidyanathan and A. T. Azar, Eds. *Backstepping Control of Nonlinear Dynamical Systems*. New York, NY, USA: Elsevier, 2020.
[23] D. Xu, Y. Dai, C. Yang, and X. Yan, "Adaptive fuzzy sliding mode command-filtered backstepping control for islanded PV microgrid with energy storage system," *J. Franklin Inst.*, vol. 356, no. 4, pp. 1880–1898, 2019.
[24] A. Basri, A. R. Husain, and K. A. Danapalasingam, "Robust chattering free backstepping sliding mode control strategy for autonomous quadrotor helicopter," *Int. J. Mech. Mechatronics Eng.*, vol. 14, no. 3, pp. 36–44, 2014.
[25] H. M. M. Adil, S. Ahmed, and I. Ahmad, "Control of maglev system using supertwisting and integral backstepping sliding mode algorithm," *IEEE Access*, vol. 8, pp. 51352–51362, 2020.
[26] T. K. Roy, M. A. Mahmud, and A. M. T. Oo, "Robust adaptive backstepping excitation controller design for higher-order models of synchronous generators in multimachine power systems," *IEEE Trans. Power Syst.*, vol. 34, no. 1, pp. 40–51, Jan. 2019.
[27] D. Zholtayev, M. Rubagotti, and T. D. Do, "Adaptive super-twisting sliding mode control for maximum power point tracking of PMSG-based wind energy conversion systems," *Renewable Energy*, vol. 183, pp. 877–889, 2022.
[28] B. Schumm, "Fuel cell," Encyclopædia Britannica, Chicago, IL, USA, Jan. 21, 2021, Accessed: Apr. 7, 2021. [Online]. Available: https://www.britannica.com/technology/fuel-cell
[29] M. Blal, A. Benatiallah, A. NeÇaibia, S. Lachtar, N. Sahouane, and A. Belasri, "Contribution and investigation to compare models parameters of (PEMFC), comprehensives review of fuel cell models and their degradation," *Energy*, vol. 168, pp. 182–199, 2019.
[30] X. Chen *et al.*, "Thermodynamic and economic study of PEMFC stack considering degradation characteristic," *Energy Convers. Manage.*, vol. 235, 2021, Art. no. 114016.
[31] S.-W. Tsai and Y.-S. Chen, "A mathematical model to study the energy efficiency of a proton exchange membrane fuel cell with a dead-ended anode," *Appl. Energy*, vol. 188, pp. 151–159, 2017.
[32] A. de Bernardinis, M.-C. Pera, J. Garnier, D. Hissel, G. Coquery, and J.-M. Kauffmann, "Fuel cells multi-stack power architectures and experimental validation of 1 kW parallel twin stack PEFC generator based on high frequency magnetic coupling dedicated to on board power unit," *Energy Convers. Manage.*, vol. 49, no. 8, pp. 2367–2383, 2008.
[33] E. H. Houssein, A. G. Gad, K. Hussain, and P. N. Suganthan, "Major advances in particle swarm optimization: Theory, analysis, and application," *Swarm Evol. Comput.*, vol. 63, 2021, Art. no. 100868.

Xinyang Hao (Graduate Student Member, IEEE) was born in Shanxi, China. He received the B.Eng. degree in electrical engineering and automation from Shanxi University, Taiyuan, China, in 2015, and the M.Eng. degree in electrical engineering from Northwestern Polytechnical University, Xi'an, China, in 2018. He is currently working toward the Ph.D. degree with FEMTO-ST Institute, University of Technology of Belfort-Montbéliard, Belfort, France.

His research interests include advanced control of power converters and fuel cell system.

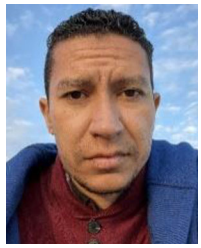

Issam Salhi (Member, IEEE) received the master's degree in control system engineering, the Ph.D. degree in electrical engineering, and the Accreditation to Supervise Research (HDR) degree in electrical engineering all from Cadi Ayyad University, Marrakesh, Morocco, in 2006, 2010, and 2016, respectively.

In 2010, he was an Associate Professor with Cadi Ayyad University. Since September 2021, he has been an Associate Professor with Energy Department, University of Technology of Belfort-Montbéliard, Belfort, France, and a member with FEMTO-ST Institute. His main research fields include fuel cells for transportation, green hydrogen production, modern control of nonlinear systems (mainly renewable energy systems), and dc/dc converters design, analysis, and control.

Salah Laghrouche received the engineer's degree in electrical engineering from the University of Algiers, Algiers, Algeria, in 2000, the Ph.D. degree in automatic and applied computer from Ecole Centrale de Nantes, Nantes, France, in 2004, and the Accreditation to Supervise Research (HDR) degree in control science from Université Paris-Sud, Paris, France, in 2014.

From 2005 to 2006, he was a Research Fellow with Laboratoire des Signaux et Systèmes, Centrale Supelec, Gif-sur-Yvette, France. Since 2006, he has been an Associate Professor of control engineering with Université de technologie de Belfort-Montbéliard, Université Bourgogne Franche-Comté, Belfort, France. He has directed numerous National and European projects and has the experience of working with global, leading industrial partners. His research interests include variable structure systems, automotive and fuel cell control systems, renewable and smart energy management and power systems.

Dr. Laghrouche is an Editorial Board Member for the IEEE/ASME TRANSACTIONS ON MECHATRONICS, *International Journal of Robust and Nonlinear Control*, *Journal of The Franklin Institute*, *International Journal of Systems Science*, and *Asian Journal of Control*. He is a member of the Conference Editorial Board of the IEEE Control Systems Society.

Youcef Ait-Amirat received the Dipl.Ing. degree from Ecole Nationale Polytechnique, Alger, Algeria, in 1989, and the Ph.D. degree from the University of Claude-Bernard, Lyon, France, in 1994.

Since 1995, he has been an Associate Professor with the University of Franche-Comté, Belfort, France. His research interests include control engineering and system theory, in particular, control of electrical systems, power and energy management of systems in line with the goal of zero carbon emissions, whether for mobile or stationary applications.

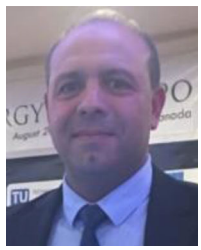

Abdesslem Djerdir was born on August 5, 1969. He received the B.S. degree from the National Institute of Electrical Engineering, Bejaia, Algeria, in 1993, and the Ph.D. degree from the University of Franche-Comté, Belfort, France, in 1999, both in electrical engineering.

He is currently a Full Professor with the University of Technology Belfort-Montbéliard (UTBM), Belfort, France. Since December 2014, he has been the Head of the Energy Department, UTBM. His research interests include modeling and design of electric and fuel cell vehicle systems (electrical machines, energy storage devices, and power converters). He develops his main research articles on availability and high efficiency of electric drive trains for transport applications by combining the experimental and theoretical approaches. In this framework, he was the Vehicle Referent of the Mobypost Project (http://mobypost-project.eu) where ten fuel cell electrical vehicles were built and tested.

Dr. Djerdir was the recipient of the International Conference on Electrical Machines Best Conference Paper Award in 1998.